

Topology detection in cavity QED

Beatriz Pérez-González,¹ Álvaro Gómez-León,² and Gloria Platero¹

¹*Instituto de Ciencia de Materiales de Madrid (ICMM, CSIC)*

²*Instituto de Física Fundamental (IFF, CSIC)*

We explore the physics of topological lattice models in c-QED architectures for arbitrary coupling strength, and the possibility of using the cavity transmission as a topological marker. For this, we develop an approach combining the input-output formalism with Mean-Field theory, which includes self-consistency and quantum fluctuations to first order, and allows to go beyond the small-coupling regime. We apply our formalism to the case of a fermionic Su-Schrieffer-Heeger (SSH) chain. Our findings confirm that the cavity can indeed act as a quantum sensor for topological phases, where the initial state preparation plays a crucial role. Additionally, we discuss the persistence of topological features when the coupling strength increases, in terms of an effective Hamiltonian, and calculate the entanglement entropy. Our approach can be applied to other fermionic systems, opening a route to the characterization of their topological properties in terms of experimental observables.

I. INTRODUCTION

Cavity Quantum Electro-Dynamics (c-QED) studies the interaction between light and matter at the most elementary level, either with individual atoms [1] or solid-state devices, like mesoscopic circuits [2]. Hybrid systems host unique fundamental phenomena due to the appearance of collective light-matter excitations [3], and have revealed themselves as an important tool for the control and manipulation of quantum systems [4]. In particular, they have become an essential landmark in the development of quantum technologies, such as quantum computing [5, 6] or quantum information processing [7]. This is because the coherent interaction of both systems allows for an efficient transfer of information between the two [8, 9], provided that the coupling with the cavity is larger than the losses in the system.

A step further can be taken by considering the combination of quantum light and complex quantum materials with emergent properties, being topological systems an outstanding example [10–13]. Topological phases of matter are characterized by a topological invariant which takes integer values, and whose associated physical properties are robust against a wide number of perturbations. A well-known example are topological insulators (TIs). They have mid-gap states which are exponentially localized at the boundaries and protected by the topological properties of the band structure.

In c-QED experiments, one typically sends an input signal through the transmission line and detects the output, once the photons have interacted with the quantum system placed in the cavity. The complex transmission coefficient $t_c = |t_c|e^{i\varphi}$ characterizes the photon propagation, and contains information about the system inside the cavity. As knowledge of the input and output fields is experimentally available, input-output theory [14, 15] has become a useful tool to predict the physics of these experiments, given its simplicity to obtain the cavity transmission as the ratio of the

output and input fields $t_c = \langle b_{\text{out}} \rangle / \langle b_{\text{in}} \rangle$. The standard input-output formalism has been specially applied in the context of linear interaction with the cavity photons and small coupling, although some generalizations have been considered as well [19, 20].

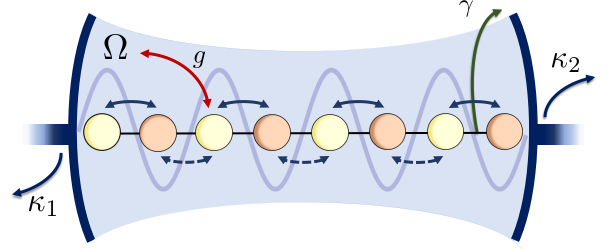


Figure 1: **System Schematic.** Schematic picture of a dimerized chain interacting with the photons in a cavity. The cavity photons have frequency Ω and are connected to the input and output ports $l = 1, 2$ with factors κ_i ($i = 1, 2$). The fermions interact with the photons with strength g and γ represents the spectral broadening of the fermionic system.

In this work, we investigate the physics of fermionic topological systems placed in c-QED architectures and explore the cavity transmission for different coupling strength. Specifically, we consider the case of a one-dimensional chain described by the SSH model [16–18] interacting with a single-mode cavity, with the losses of the system being always smaller than the interaction strength. Our aim is to investigate the use of the cavity transmission as a topological marker, and characterize the physics of the hybrid system.

For that purpose, we develop a formalism to calculate t_c for arbitrary coupling in terms of the retarded photonic Green function (GF). GFs have the advantage that can be exactly obtained using numerical techniques, with the eigenvectors and eigenvalues of the total Hamiltonian. We also obtain an analytical expression for the cavity transmission through a generalized input-output formal-

ism, using a mean-field (MF) plus fluctuations analysis, and discuss its validity for different coupling strengths. We find that the transmission can be used to detect non-trivial topology in a fermionic system, with an appropriate state preparation depending on the regime considered. We also derive an effective Hamiltonian to investigate the topological changes produced by the hybridization between photons and fermions, and obtain the entanglement entropy for different partitions of the system.

II. THEORY

A. Mean-field and fluctuations approach

We consider a mesoscopic system interacting with a cavity, with the following Hamiltonian

$$H = H_0 + V + H_B, \quad (1)$$

with $H_0 = H_S + \Omega d^\dagger d$, where H_S describes the single-particle physics of a topological system (which we leave undetermined for the moment) and the second term corresponds to the cavity Hamiltonian, being d (d^\dagger) the destruction (creation) photon operator. The interaction term in Eq.1 is assumed to have the following form $V = g(d^\dagger + d)Z$, with Z being the fermionic coupling operator, while H_B accounts for the quantized electromagnetic field outside the cavity and its linear coupling with the cavity photons [15]:

$$H_B = \sum_{l=1,2} \int_{-\infty}^{\infty} \omega b_l^\dagger(\omega) b_l(\omega) d\omega + i \sum_{l=1,2} \int_{-\infty}^{\infty} [\mu_l(\omega) b_l^\dagger(\omega) d - \mu_l(\omega)^* d^\dagger b_l(\omega)] d\omega \quad (2)$$

where $l = 1, 2$ represent the left/right sides of the cavity, $b_l(\omega)$ is the destruction operator for a photon with energy ω at side l of the cavity and μ_l represents the coupling between the cavity and the outside modes.

In this work, we apply a MF decoupling and write each operator in V as its average plus the fluctuations around it: $\mathcal{O} = \langle \mathcal{O} \rangle + \delta \mathcal{O}$, being $\delta \mathcal{O}$ the fluctuations operator. This results in the following Hamiltonian for the cavity and fermionic system:

$$H_0 + V = H_S + g(\langle d^\dagger \rangle + \langle d \rangle) Z + \Omega d^\dagger d + g \langle Z \rangle (d^\dagger + d) + g(\delta d^\dagger + \delta d) \delta Z \quad (3)$$

The first and the second line in Eq.3 contain the fermionic and photonic MF Hamiltonians, respectively. The third line in Eq.3 contains the fluctuations (which we will denote fluctuations Hamiltonian H_δ hereafter), while the scalar contribution can be neglected. Note that the bath Hamiltonian H_B has not been included in Eq.3, since its coupling to the cavity is very weak and no backaction between subsystems is expected. Also, the linear terms in the fluctuations operators (i.e. terms containing fluctuation operators only from one of the subsystems) have been rewritten in terms of the original ones.

In the asymptotic limits of $g \rightarrow \{0, \infty\}$, fluctuations are completely suppressed and the two systems effectively decouple, making the MF description exact. However, away from these limits, fluctuations are relevant and must be estimated, at least to leading order.

Physically, one can see in Eq.3 that if $\langle d \rangle, \langle d^\dagger \rangle \neq 0$, the cavity photons introduce a term proportional to Z in the fermionic Hamiltonian, that can affect the topological properties. Similarly, for $\langle Z \rangle \neq 0$ the photonic part acquires a term analogous to an external field coupled to the photons. Therefore, for a complete characterization one needs to find self-consistent solutions to $\langle Z \rangle, \langle d^\dagger \rangle$ and $\langle d \rangle$, which can be easily obtained, to lowest order, from the MF Hamiltonian. To do so, we rotate the photonic MF Hamiltonian $H_\Omega = \Omega d^\dagger d + g(d^\dagger + d)\langle Z \rangle$ with $R = \exp\{-g\langle Z \rangle(d^\dagger - d)/\Omega\}$, diagonalizing it to the form

$$\tilde{H}_\Omega = R^\dagger H_\Omega R = \Omega d^\dagger d - \frac{g^2 \langle Z \rangle^2}{\Omega} \quad (4)$$

As expected, Eq.4 indicates that, at the MF level, the solely effect of the topological system on the cavity photons is a global shift of all their energies. Importantly, Eq.4 allows to determine the average of the photon operators, resulting in:

$$\langle d^\dagger \rangle + \langle d \rangle = -2 \frac{g}{\Omega} \langle Z \rangle \quad (5)$$

Using Eq.5, the MF fermionic Hamiltonian can be written in terms of fermionic averages only:

$$\tilde{H}_S = H_S - 2 \frac{g^2}{\Omega} \langle Z \rangle Z. \quad (6)$$

This simplifies the calculation of the self-consistency equation for $\langle Z \rangle$, which can now be obtained using an iterative numerical procedure in terms of Hubbard operators: $\tilde{X}^{\tilde{\alpha}} = \tilde{X}^{\alpha_1, \alpha_2} = |\tilde{\alpha}_1\rangle \langle \tilde{\alpha}_2|$, with $|\tilde{\alpha}_i\rangle$ ($\alpha_i = 1, \dots, N$) being the eigenstates of the MF fermionic Hamiltonian,

$\tilde{H}_S|\tilde{\alpha}_i\rangle = \tilde{E}_{\alpha_i}|\tilde{\alpha}_i\rangle$, and $\vec{\alpha} = (\alpha_1, \alpha_2)$. We also write the fluctuations Hamiltonian in this basis, and rotate the photonic part with R , to find:

$$\tilde{H}_\delta = R^\dagger H_\delta R = g (d^\dagger + d) \sum_{\vec{\alpha}} \tilde{Z}_{\vec{\alpha}} \tilde{X}^{\vec{\alpha}}, \quad (7)$$

where $\tilde{Z}_{\vec{\alpha}} = \langle \tilde{\alpha}_1 | (Z - \langle Z \rangle) | \tilde{\alpha}_2 \rangle$.

B. Cavity transmission and photonic Green's function

In this section, we demonstrate a connection between the retarded photonic Green function $G(t, t') = -i\theta(t - t')\langle [d(t), d^\dagger(t')] \rangle$ and the cavity transmission t_c . The starting point is the Langevin equation for the cavity field $d(t)$ [5, 15]:

$$\begin{aligned} \partial_t d(t) = & -i \left(\Omega - i\frac{\kappa}{2} \right) d(t) - \sum_{l=1,2} \sqrt{\kappa_l} \tilde{b}_{\text{in},l}(t) \\ & - ig \sum_{\vec{\alpha}} \tilde{Z}_{\vec{\alpha}} \tilde{X}^{\vec{\alpha}}(t), \end{aligned} \quad (8)$$

where we have considered the Markov approximation $\mu_l(\omega) = \sqrt{\kappa_l}/2\pi$ and defined $\kappa = \kappa_1 + \kappa_2 = \Omega/Q$, with Q being the cavity quality factor. The term $\tilde{b}_{\text{in},l}(t)$ corresponds to the input fields from both sides l of the cavity, in the rotated frame. From the reversed-time equation of motion (EoM) one can find the input-output relation $\tilde{b}_{\text{out},l}(t) = \tilde{b}_{\text{in},l}(t) + \sqrt{\kappa_l}d(t)$ [73]

Now, it is only required to notice that $G(t, t')$, whose EoM yields

$$\begin{aligned} i\partial_t G(t, t') = & \left(\Omega - i\frac{\kappa}{2} \right) G(t, t') + \delta(t - t') \\ & - ig\theta(t - t') \sum_{\vec{\alpha}} Z_{\vec{\alpha}} \langle [\tilde{X}^{\vec{\alpha}}(t), d^\dagger(t')] \rangle, \end{aligned} \quad (9)$$

is the resolvent of Eq. (8). In Fourier space, this means we can write the photonic operator $d(\omega)$ as

$$d(\omega) = -iG(\omega) \sum_{l=1,2} \sqrt{\kappa_l} \tilde{b}_{\text{in},l}(\omega). \quad (10)$$

Again, a complete derivation of Eq. 10 can be found in the Supplemental Material [73]. Then, using the previous expression and the input-output relation, one can easily see that

$$t_c(\omega) = \frac{\langle \tilde{b}_{\text{out},2} \rangle}{\langle \tilde{b}_{\text{in},1} \rangle} = -i\sqrt{\kappa_1\kappa_2}G(\omega), \quad (11)$$

where we have assumed the input is only through port 1. This is a key result, since Eq.11 holds for arbitrary values of the coupling constant g . Although an analytical expression for $G(\omega)$ is not possible to achieve for all g , an exact numerical result can always be obtained using the eigenvalues and eigenvectors of the total Hamiltonian.

C. Analytical result

One can see in Eq. 8 that, as the cavity photons couple to the fermionic system, the presence of the term $-ig \sum_{\vec{\alpha}} \tilde{Z}_{\vec{\alpha}} \tilde{X}^{\vec{\alpha}}(t)$ connects the topological properties of the later with the output photons detected at the ports of the transmission line. The equation of motion for the Hubbard operator yields:

$$\begin{aligned} \partial_t \tilde{X}^{\vec{\alpha}}(t) = & i \left(\tilde{E}_{\vec{\alpha}} - i\frac{\gamma}{2} \right) \tilde{X}^{\vec{\alpha}}(t) \\ & + ig (d^\dagger(t) + d(t)) \sum_{\beta} \left(\tilde{Z}_{\beta, \alpha_1} \tilde{X}^{\beta, \alpha_2}(t) \right. \\ & \left. - \tilde{Z}_{\alpha_2, \beta} \tilde{X}^{\alpha_1, \beta}(t) \right), \end{aligned} \quad (12)$$

where $\tilde{E}_{\vec{\alpha}} = \tilde{E}_{\alpha_1} - \tilde{E}_{\alpha_2}$, and the phenomenological spectral broadening γ is considered to be equal for all electronic transitions. To close the system of equations and find an analytical solution for $d(\omega)$, a decoupling scheme is required. In this context, we notice that contributions from fluctuations are small in the regimes $g \ll \Omega, \tilde{E}_{\vec{\alpha}}$ and $g \gg \Omega, \tilde{E}_{\vec{\alpha}}$. Under these conditions, we can rewrite the product $d^{(\dagger)}(t)\tilde{X}^{\vec{\alpha}}(t)$ as

$$d^{(\dagger)}(t)\tilde{X}^{\vec{\alpha}}(t) \approx \langle \tilde{X}^{\vec{\alpha}} \rangle d^{(\dagger)}(t) + \langle d^{(\dagger)} \rangle \tilde{X}^{\vec{\alpha}}(t), \quad (13)$$

where we neglect extra correlation terms introduced by the fluctuations Hamiltonian, which acts as an effective interaction between the two MF Hamiltonians. The expected values $\langle d^{(\dagger)} \rangle$ and $\langle \tilde{X}^{\vec{\alpha}} \rangle$ can then be calculated using the MF Hamiltonians for the cavity and fermionic system, respectively, as shown in the previous section. As a result, the photonic averages *in the rotated frame* can be taken to be $\langle d^{(\dagger)} \rangle \sim 0$. We will also neglect the contribution $\langle \tilde{X}^{\vec{\alpha}} \rangle d^{(\dagger)}(t)$ for being small in the regime of interest [21].

With these approximations, we find the solution for the Hubbard operator,

$$\tilde{X}^{\bar{\alpha}}(\omega) \simeq \frac{gd(\omega)}{\omega + \tilde{E}_{\bar{\alpha}} - i\frac{\gamma}{2}} \sum_{\beta} \left(\tilde{Z}_{\alpha_2, \beta} \langle \tilde{X}^{\alpha_1, \beta} \rangle - \tilde{Z}_{\beta, \alpha_1} \langle \tilde{X}^{\beta, \alpha_2} \rangle \right), \quad (14)$$

This leads to the following expression for the cavity operator:

$$d(\omega) \simeq \frac{i \left(\sqrt{\kappa_1} \tilde{b}_{\text{in},1} + \sqrt{\kappa_2} \tilde{b}_{\text{in},2} \right)}{\Omega - \omega + g^2 \tilde{\chi}(\omega) - i\frac{\kappa}{2}}. \quad (15)$$

where

$$\tilde{\chi}(\omega) = \sum_{\bar{\alpha}\beta} \tilde{Z}_{\bar{\alpha}} \frac{\left(\tilde{Z}_{\alpha_2, \beta} \langle \tilde{X}^{\alpha_1, \beta} \rangle - \tilde{Z}_{\beta, \alpha_1} \langle \tilde{X}^{\beta, \alpha_2} \rangle \right)}{\omega + \tilde{E}_{\bar{\alpha}} - i\frac{\gamma}{2}}. \quad (16)$$

Eq.15 is analogous to what one would find for the small- g regime in the standard input-output formalism [21], with the difference that in this case all fermionic parameters are renormalized by the MF self-consistency equations, and that allows to extend the validity of the solution to both the small- g and very-large- g regimes [73]. Finally, if we consider the input-output relation, we find that the cavity transmission is given by:

$$t_c = \frac{\langle \tilde{b}_{\text{out},2} \rangle}{\langle \tilde{b}_{\text{in},1} \rangle} = \frac{i\sqrt{\kappa_1\kappa_2}}{\Omega - \omega + g^2 \tilde{\chi}(\omega) - i\frac{\kappa}{2}} \quad (17)$$

where we can now identify $\tilde{\chi}(\omega)$ as the usual electronic susceptibility [21]. In the region of validity of Eq. 17, the statistical averages for the Hubbard operators can be approximated by their unperturbed values $\langle \tilde{X}^{\bar{\alpha}} \rangle = \delta_{\alpha_1, \alpha_2} p_{\alpha_1}$, being p_{α} the occupation of state $|\bar{\alpha}\rangle$ in the fermionic density matrix $\rho_f = \sum_{\alpha} p_{\alpha} \tilde{X}^{\alpha, \alpha}$. Then, the electronic susceptibility can be written as:

$$\tilde{\chi}(\omega) = \sum_{\bar{\alpha}} \frac{|\tilde{Z}_{\bar{\alpha}}|^2 p_{\bar{\alpha}}}{\omega + \tilde{E}_{\bar{\alpha}} - i\gamma_{\bar{\alpha}}}, \quad (18)$$

with $|\tilde{Z}_{\bar{\alpha}}| = \tilde{Z}_{\alpha_1, \alpha_2} \tilde{Z}_{\alpha_2, \alpha_1}$, and $p_{\bar{\alpha}} = p_{\alpha_1} - p_{\alpha_2}$.

Similarly, using the same manouvres and approximations as for the calculation of $d(\omega)$ above, one obtains the following expression for the photonic Green function in the case of $g \ll \Omega, \tilde{E}_{\bar{\alpha}}$ and $g \gg \Omega, \tilde{E}_{\bar{\alpha}}$:

$$G(\omega) = -\frac{1}{\Omega - \omega + g^2 \tilde{\chi}(\omega)}. \quad (19)$$

It is straight-forward to see that the previous expression verifies the relation between the transmission and $G(\omega)$ presented in Eq. 11, when compared with Eq. 17 in the limits of $g \ll \Omega, \tilde{E}_{\bar{\alpha}}$ and $g \gg \Omega, \tilde{E}_{\bar{\alpha}}$.

As $G(\omega)$ can in general be calculated numerically using exact diagonalization, we can employ Eq.11 to check the accuracy of the analytical result for t_c obtained in Eq.17 for both the small- and very-large- g regimes, as will be shown in the section below. Furthermore, we will interpolate Eq.17 to the intermediate regime of interaction, in which fluctuations have a crucial contribution. The validity of Eq. 17 away from the regions $g \ll \Omega, \tilde{E}_{\bar{\alpha}}$ and $g \gg \Omega, \tilde{E}_{\bar{\alpha}}$ is tested by comparing with Eq. 11, and also by deriving an effective Hamiltonian that will be presented in a later section. Regarding the resonant case, deriving an analytical result for the transmission that captures the physics of the system beyond the small- g regime would require additional considerations, such as the employment of the rotating wave approximation upon the Hamiltonian, in the spirit of the Jaynes-Cummings model. Being this out of the scope of the present work, a preliminary result can be obtained using Eq. 17, that is shown in [73].

III. RESULTS

Now we apply our formalism to a fermionic 1D topological system described by a tight-binding Hamiltonian with N sites $H_S = \sum_{(i,j)=1}^N t_{ij} c_i^{\dagger} c_j$, where t_{ij} is the hopping amplitude and c_i (c_i^{\dagger}) is the destruction (creation) operator for a spinless fermion at site i . Particularizing for the SSH model, a dimerized lattice with alternating hopping pattern, we define the intra- and inter-dimer hopping amplitudes $t = t_0(1 + \delta)$ and $t' = t_0(1 - \delta)$, respectively, with $\delta \in [-1, 1]$. Despite its simplicity, this bipartite structure captures the relevant features of non-trivial topology and gives rise to two distinct topological phases: the trivial phase ($\delta < 0$), which corresponds to the usual two-band insulator, and the topological phase ($\delta > 0$), hosting the aforementioned edge states [16–18].

For the interaction between the cavity and the chain we consider the dipolar approximation, which couples the cavity electric field to the charge density at each site $Z = \sum_i^N x_i c_i^{\dagger} c_i$, being x_i the position in the lattice [22]. In this case, the length of the chain can be comparable to the wavelength of the electric field of the cavity, which is why each site couples differently to it. Hereafter we consider the origin of positions to be found at the middle of the chain, so that $x_N = -x_1$.

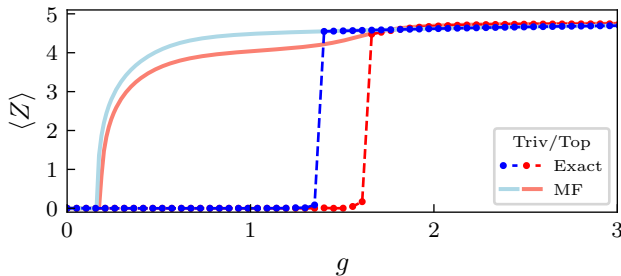


Figure 2: $\langle Z \rangle$ as a function of the coupling constant g . The value of $\langle Z \rangle$ has been calculated self-consistently using mean field (solid) and exact diagonalization (dots, including a dashed line for clarity). The parameters chosen are: $\Omega = 10$, $\delta = \pm 0.6$ (trivial/topological phase) and $N = 20$.

First, we focus on the cases $g \gg \Omega$, $\tilde{E}_{\bar{\alpha}}$ and $g \ll \Omega$, $\tilde{E}_{\bar{\alpha}}$, where quantum fluctuations are small. To estimate with more precision the region of validity of our approximation, we solve the self-consistency equation for the order parameter $\langle Z \rangle = \sum_{\bar{\alpha}} \tilde{Z}_{\bar{\alpha}} \langle \tilde{X}^{\bar{\alpha}} \rangle$. We iterate until convergence using the eigenstates of the MF Hamiltonian \tilde{H}_S in Eq. 6, and also those of the total Hamiltonian $\tilde{H}_{\delta} + \tilde{H}_S + \tilde{H}_{\Omega}$ to compare with the exact value.

Fig. 2 shows $\langle Z \rangle$ as a function of g for the mean field case and the exact one, and provides us a precise value for the breakdown of the approximation. As expected, the MF agrees with the exact value at small and large g . In the former case, $\langle Z \rangle = 0$ indicates that the MF Hamiltonian coincides with the free Hamiltonian, and that the symmetries of the model are unaffected by the coupling with the cavity. In the latter, the system polarizes (i.e., $\langle Z \rangle \neq 0$) indicating that the ground state of the system is modified and that certain symmetries change. For intermediate values, fluctuations take over and lead to disagreement between the MF and the exact solution. The MF result indicates that the change in $\langle Z \rangle$ is continuous, corresponding to a second-order phase transition. However, the exact calculation shows a discontinuity, which could indicate that is in fact a first order transition.

Interestingly, we find that beyond the critical point a difference between the topological and the trivial phase arises, which is also captured by the MF solution. This is a consequence of the different coupling between bulk/edge modes and the cavity photons. It also indicates that certain features of the topological edge states still remain when the coupling strength is increased beyond the small g regime, but they disappear again at very large g .

Also, we find that $\langle Z \rangle$ depends on the chain length N . This is intuitive due to the position-dependent interaction [73]: the chain size modifies the value of the critical

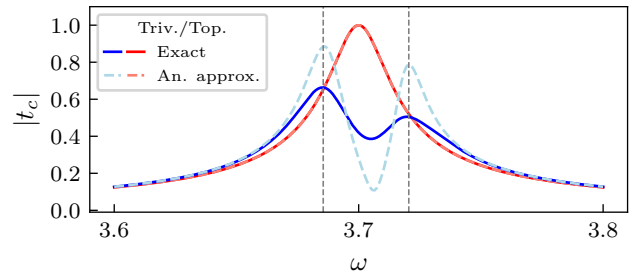


Figure 3: $|t_c(\omega)|$ and $\varphi(\omega)$ as a function of ω . Dashed lines indicate the analytical approximation (Eq. 17), while solid lines correspond to the exact solution (Eq. 11). We consider the $(N/2)$ -th state occupied, corresponding to the edge state in the topological phase and the top of the valence band in the trivial phase. The parameters used are: $\Omega = 3.7$, $g = 0.06$, $\delta = \pm 0.925$ (trivial/topological phase, in blue/red, respectively), and $N = 20$

point at which the system polarizes, enhancing or reducing the difference between topological phases at the phase transition, as well as the final value in the limit $g \rightarrow \infty$.

A. Small- g regime

The expression for the transmission (Eq.17) is easier to interpret in the regime $g \ll \Omega$, $|t_{ij}|$ because the eigenstates of \tilde{H}_S coincide with those of H_S ($\tilde{E}_{\bar{\alpha}} \rightarrow E_{\bar{\alpha}}$, $\tilde{X}^{\bar{\alpha}} \rightarrow X^{\bar{\alpha}}$) and \tilde{H}_{δ} turns into the original V (i.e. $\tilde{Z} \rightarrow Z$). The calculation of the matrix elements $Z_{\bar{\alpha}}$ shows that in a finite system, the cavity can mediate transitions between all eigenstates of the chain, with the exception of the edge states in the topological phase, which exponentially suppress their coupling with the bulk states as a function of the chain length. In consequence, if the system is initially prepared in a bulk state, t_c will change for a wide range of ω in both phases, and the cavity transmission cannot be used as a topological marker.

On the contrary, if the edge state is initially occupied in the topological phase, the transmission peak at $\omega = \Omega$ should remain unaffected by the interaction, as opposed to the behaviour of the trivial phase, in which changes in t_c are expected. This asymmetry between phases can be maximized if the cavity frequency Ω is resonant with an electronic transition $E_{\bar{\alpha}}$ (eigenenergy of the unperturbed fermionic Hamiltonian H_S) and in particular, with the gap of the chain. While the transmission for the non-trivial topological phase does not change compared to the uncoupled cavity transmission (the bulk states are decoupled from the edge states), the presence of a direct resonance in the trivial phase results in a Rabi splitting: the peak of maximum transmission divides into two distinct modes, separated by the Rabi frequency Ω_r [23], which is often detected in experiments by measuring the transmission amplitude, and indicates that the regime

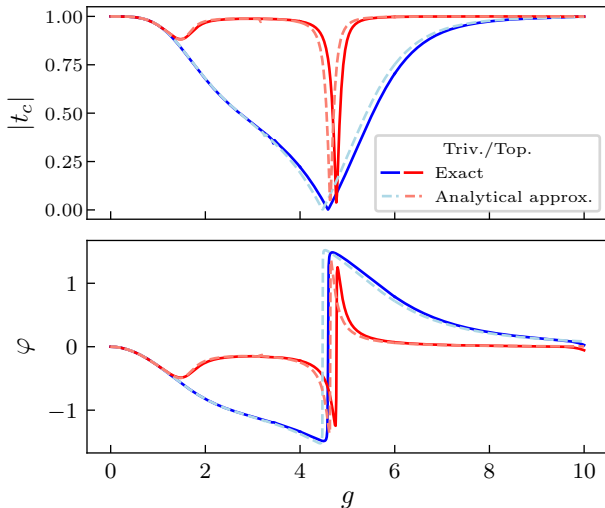


Figure 4: $|t_c(\omega)|$ and φ as a function of g . Dashed lines indicate the solution from the analytical approximation (Eq. 17), while solid lines correspond to the exact solution (Eq. 11). We consider that the ground state of the chain ($N = 20$) is occupied. The parameters used are: $\Omega = 10$, $|\delta| = 0.6$

$g > \{\kappa, \gamma\}$ is achieved [24–28].

This is shown in Fig. 3. We consider the top state in the valence band is occupied for the trivial phase, while the edge state is occupied for the topological phase. This choice is motivated by the fact that both states are adiabatically connected across the topological phase transition, as δ is varied from negative to positive values. While the decoupling between bulk and edge states explains the absence of any changes in t_c for the topological phase, a Rabi splitting appears for the trivial phase. The analytical approximation captures the position of each peak in ω (as indicated by the dashed, grey vertical lines), as well as their relative height, though the exact shape of the peaks is not reproduced. This disagreement can be explained by the existence of correlated excitations that strongly modify the system due to the presence of direct electronic transitions. Additionally, the parameters have to be chosen such that $g^2\chi(\omega)$ in Eq. 16 is non-divergent, which is not a problem in the off-resonant case.

In conclusion, for the small- g regime it is important to stress that detection of the topological phase requires the system to be initialized in an edge state. Otherwise the cavity transmission cannot differentiate between the two phases.

B. Beyond the small- g regime

We now consider the opposite limit, where $g \gg \Omega$, $|t_{i,j}|$ and the order parameter $\langle Z \rangle \neq 0$. In this case the MF eigenstates do not coincide with the unperturbed ones, as the MF correction does not commute with the original Hamiltonian. Now each site has different energy due to the contribution of the term $-2g^2\langle Z \rangle Z/\Omega$ in \tilde{H}_S (Eq. 6) and the states tend to localize, breaking the original chiral symmetry of the SSH model and destroying the topological order. This is analogous to the Wannier-Stark effect in the presence of a classical DC field. On the other hand, the energy of the cavity photons globally shifts (Eq. 4), which means we expect to measure $|t_c| \simeq 1$ again for very large g (i.e. when the photons are largely detuned).

This is shown in Fig. 4, where we have calculated the transmission at $\omega = \Omega$ for both phases, as a function of the coupling strength g . This includes both the small- g and very-large- g regimes, as well as the interpolation for intermediate coupling strengths. We have chosen $\Omega = 10$, which is far from any resonance with the electronic system.

First, note that the comparison between Eqs. 17 and 11 gives a perfect agreement between the exact numerical result and the analytical approximation for arbitrary g , which means that Eq. 17 captures the behaviour of the system for arbitrary coupling.

Second, *the calculations are made considering the chain in its ground state*. For small g , both phases show the same behaviour, as expected: the peak of maximum transmission, initially found at $\omega = \Omega$, shifts due to the interaction. Then, Eqs. 17 and 11 predict that the break-down of the small- g regime brings essential differences between the trivial and topological phase, that are enhanced with the interaction: while the trivial phase decays monotonically until reaching a minimum, the topological phase remains mostly unaffected, except for a notorious dip in $|t_c|$ (which corresponds to a change of sign in φ). This is unexpected, as perturbation theory predicts a suppression of the hopping for increasing g and the fast destruction of the topological phase. Thus, the effect of the topological edge states is not washed away by the chiral-symmetry breaking, and the difference between phases can still be detected. Finally, both phases display perfect transmission when g is sufficiently large, in accordance with the MF result.

IV. TOPOLOGICAL FEATURES

A. Effective Hamiltonian

To explore in more detail the different interaction regimes and the persistence of edge states beyond small coupling, we derive an effective Hamiltonian using a Schrieffer-

Wolff transformation in the mean field basis, where the fluctuations Hamiltonian \tilde{H}_δ is considered the perturbation to $\tilde{H}_S + \tilde{H}_\Omega$. We propose the following ansatz for the transformation:

$$S = g \sum_{i,j} \left(\frac{x_{ij} t_{ij}}{\Omega^2 - 2g^2 \langle Z \rangle x_{ij}} d^\dagger + \frac{x_{ij} t_{ij}}{\Omega^2 + 2g^2 \langle Z \rangle x_{ij}} d \right) c_i^\dagger c_j + \frac{g}{\Omega} (d^\dagger - d) (Z - \langle Z \rangle) \quad (20)$$

where $x_{ij} = x_i - x_j$. Then, the effective Hamiltonian $\bar{H} = e^S \tilde{H} e^{-S} \simeq \tilde{H}_S + \tilde{H}_\Omega + \frac{1}{2} [S, \tilde{H}_\delta]$ results in the following approximate form [73]:

$$\bar{H} \simeq \sum_{i,j} \bar{t}_{i,j} c_i^\dagger c_j + \Omega d^\dagger d \left(1 - \sum_{i,j} \bar{\Omega}_{i,j} c_i^\dagger c_j \right) - \sum_{i,j} \bar{\rho}_{i,j} \{ c_i^\dagger c_j, Z \} - \frac{g^2}{2\Omega} \{ Z, Z \}, \quad (21)$$

with

$$\bar{t}_{ij} = t_{ij} \left(1 - g^2 x_{ij}^2 \frac{\Omega^2 - 2g^2 \langle Z \rangle^2}{\Omega^4 - 4g^4 \langle Z \rangle^2 x_{ij}^2} \right), \quad (22)$$

$$\bar{\Omega}_{ij} = t_{ij} \frac{\Omega g^2 x_{ij}^2}{\Omega^4 - 4g^4 \langle Z \rangle^2 x_{ij}^2}, \quad (23)$$

$$\bar{\rho}_{ij} = t_{ij} \frac{g^4 \langle Z \rangle x_{ij}^2}{\Omega^4 - 4g^4 \langle Z \rangle^2 x_{ij}^2}. \quad (24)$$

To derive Eq.E14 we have neglected the small correction provided by two-photon transitions in the rotated frame. The effective Hamiltonian \bar{H} includes renormalized hopping amplitudes \bar{t}_{ij} (Eq.22), a cavity frequency shift $\bar{\Omega}_{ij}$ (Eq.23), a density-assisted hopping $\bar{\rho}_{ij}$ (Eq.24) and a density-density interaction (last term in Eq.E14), which can be neglected for the current case of a chain with small filling (however, notice that the local term $-\frac{g^2}{2\Omega} \sum_i x_i^2 c_i^\dagger c_i$ must be kept). Note that the term $\bar{\Omega}_{ij}$ encodes the electron-photon correlations.

Importantly, the dependence of each term on $\langle Z \rangle$ makes our result non-perturbative, since $\langle Z \rangle$ is a function of the other parameters as well. Indeed, one can see that \bar{t}_{ij} has an interesting non-monotonic behavior due to the finite value of $\langle Z \rangle$ (see Fig. 5). For small g (recall that in this regime $\langle Z \rangle = 0$, see Fig. 2), the hopping is suppressed as $t_{ij} (1 - g^2 x_{ij}^2 / \Omega^2)$, indicating a tendency towards localization. This renormalization does not affect the topological properties of the chain, but the appearance of the staggered potential from the density-density

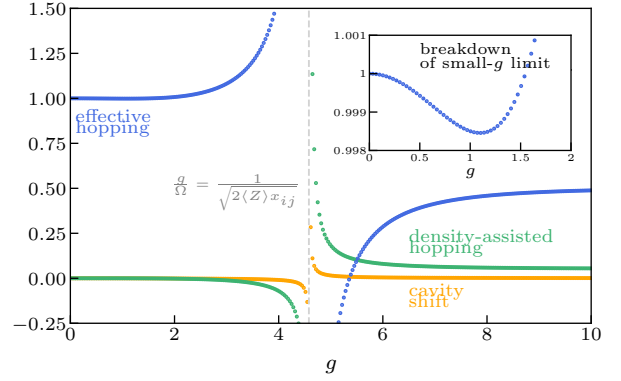


Figure 5: **Renormalized parameters in the effective Hamiltonian.** Plot of the renormalized hopping amplitude \bar{t}_{ij} (blue), cavity shift $-\bar{\Omega}_{ij}$ (yellow) and density-assisted hopping $-\bar{\rho}_{ij}$ (green) vs g , for $t_{ij} = 1$, $x_{ij} = 0.5$ (so that the length of the unit cell is the unit), and $\Omega = 10$. The minus sign in $-\bar{\rho}_{ij}$ and $-\bar{\Omega}_{ij}$ corresponds to the sign of their respective terms in the Hamiltonian (Eq. E14).

term $-\frac{g^2}{2\Omega} \sum_i x_i^2 c_i^\dagger c_i$ breaks chiral symmetry and explains the expected destruction of the topological phase. In fact, as the coupling is increased, the edge states reduce their energy gradually and eventually penetrate into the bulk bands [73].

In contrast, once the small- g regime breaks down and $\langle Z \rangle \neq 0$, the tendency to localize of \bar{t}_{ij} is reversed. This coincides with the onset of a qualitative distinct behaviour between phases with distinct topology, as shown in Fig. 4. Then, the hopping is enhanced until (see Fig. 5):

$$\frac{g}{\Omega} = (2\langle Z \rangle x_{ij})^{-1/2} \quad (25)$$

where \bar{t}_{ij} , $\bar{\Omega}_{ij}$ and $\bar{\rho}_{ij}$ simultaneously diverge. In particular, the divergence indicates a resonance between photons and fermions, which should lead to a drop in the transmission, in accordance with the minimum in Fig. 4 (plot with $\Omega = 10$) for both phases. Note also that this instability of the solution can only happen when $\langle Z \rangle \neq 0$, indicating that it is possible only beyond the small- g regime. Beyond this divergence, all terms tend to a constant value, with the hopping being reduced by half and the staggered potential which continues increasing. From this analysis we can deduce that beyond the small- g condition, there is an intermediate regime, characterized by the presence of electron-photon correlations in which the hopping is enhanced, consistent with a stabilization of the topological phase and with the nearly constant $|t_c|$ (Fig. 4) for the topological phase. This is followed by an instability for larger values of g which finally leads to a localized phase.

B. Entanglement entropy

Finally, to gain further insight into the topological features of the intermediate coupling regime, we explore the entanglement entropy in the system. The von Neumann entropy is defined as $S_A = -\text{tr}_A \rho_A \ln \rho_A$, where ρ_A corresponds to the reduced density matrix of a subsystem A . When the system is divided in two partitions $A \oplus B$, S_A measures the amount of quantum correlation between them (note that $S_A = S_B$, with S_B defined analogously). The entropy has been used in the study of quantum criticality and topology and has several contributions. In particular, in non-interacting systems one can find boundary contributions related with the Berry phase of the states and with the presence of edge modes [29].

In our case, we can partition the system in two different ways. First, we consider a partition separating the fermionic chain and the cavity, and calculate S_{fer} by tracing out the photonic degrees of freedom (Fig. 6(a)). In that case, we can see that S_{fer} grows with g and suddenly drops at a critical coupling strength value, which is different for the trivial and topological phase and reproduces the phase transition captured by the order parameter $\langle Z \rangle$ in Fig. 2. However, the differences between both phases at finite coupling are not clarified for this partition.

The alternative partition requires to first integrate out the photonic degrees of freedom. The resulting density matrix for the fermionic chain encodes the role of photons and can be divided in two parts $A = \{1, 2, \dots, N_A\}$ and $B = \{N_A + 1, N_A + 2, \dots, N\}$ (with $N_A \neq N/2$) of which the entropy can be calculated. This is interesting from a topological perspective, because the entanglement between these partitions has been already studied in non-interacting SSH chains and can differentiate between the trivial and the topological phase [29]. In our case the fermionic reduced density matrix is dressed by photons, which makes the model more interesting from a fundamental perspective, as we are dealing with many-body topological models.

In Fig. 6(b) we plot the entanglement entropy for the system in its ground state. In general, the entropy increases as a function of g for both phases and saturates to $\log 2$, dropping to zero as the expectation value $\langle Z \rangle$ acquires a finite value. In that sense its behavior is similar to that of Fig. 6(a) and can be used to obtain information about the phase diagram for the order parameter. Interestingly, the saturation to $\log 2$ indicates that the ground state becomes a cat state for finite g , which is destroyed when the system polarizes (i.e., $\langle Z \rangle \neq 0$), turning into a fully localized state. However, it does not provide new insight into the topological characterization of the system, as it only differentiates between the two phases in the range of values comprised between their respective

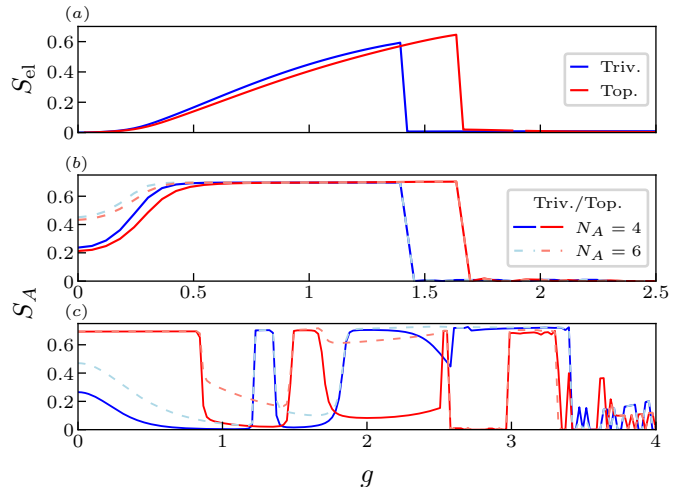


Figure 6: **Entanglement entropy for different partitions.** (a) S_{el} ($N = 20$) for the ground state, with $\Omega = 10$, $|\delta| = 0.6$, and $N = 20$. It grows as the coupling is increased, dropping to zero when the fermionic system polarizes. (b) S_A as a function of g for different partitions N_A and the system in its ground state. As in the previous case, S_A increases with the coupling until it drops to zero, reproducing the phase transition appearing in $\langle Z \rangle$ (Fig. 2). (c) S_A for the system in its $N/2$ -th state, analogous to half-filling in the non-interacting case. The topological phase initially displays a quantized value $S_A = \log 2$ independent of the partition, indicating the presence of an edge state.

critical g .

In contrast, Fig. 6(c) considers the $N/2$ -th state occupied (this is specially relevant to compare with half-filling in a non-interacting SSH chain). This state coincides with the edge state in the topological phase and with the top of the valence band in the trivial phase for the isolated chain. In this case the topological phase displays a quantized value $S_A = \log 2$ for small g , independent of the partition, while for the trivial phase S_A is smaller and changes for different partitions N_A . The $\log 2$ value is a consequence of a maximally entangled cat state and its independence on the partition indicates that it is localized at the boundaries of the system (i.e., the bulk does not contribute and all entropy comes from the entanglement between the two edges [29]). Then, we can see that the topological boundary mode is present until the entropy drops, indicating the destruction of entanglement for the $N/2$ -th state. This coincides with the first anti-crossing of the edge state with a bulk state as they penetrate in the bulk bands (shown in [73]).

The persistence of the $\log(2)$ value for S_A in the topological chain for small g means the interaction preserves the entanglement between ending sites created by the original topological boundary modes, though their energy and

localization length does change due to the symmetry-breaking terms in the effective Hamiltonian. This can have important implications for designing quantum information protocols with c-QED structures in which correlation between distant sites of the fermionic system needs to be exploited, which in this case is naturally provided by the topological features of the chain.

Importantly, the topological contribution to the entanglement does not disappear after S_A drops to zero at $g \sim 0.8$, but migrates from one state to the other as the anti-crossing originated by the edge states entering the band take place in the energy spectrum [73].

Interestingly, increasing g leads to a succession of new log 2 plateaus, indicating that boundary modes are linked with both the trivial and the topological phase [30–32]. Again, each abrupt change in S_A coincides with an anti-crossing between the $N/2$ -th and other states in the upper bands [73]. Finally, when g approaches the divergence in Fig. 5 the entropy drops for both phases and the presence of boundary modes is completely washed out by the interaction with the cavity.

The existence of edge states in the energy spectrum in both phases for large g is a consequence of the form of the fermionic coupling operator Z , which acts more strongly at the ending sites of the chain than in the middle region. It is very enlightening to compare these results with the ones obtained by setting $x_i \equiv x$ (which would be the case if the size of the fermionic system was negligible in comparison with the wavelength of the electric field in the cavity). Such a interaction model would not create any entanglement neither between photons and fermions, nor within the ending sites of the fermionic chain, and would not give rise to these log (2) plateaus.

V. EXPERIMENTAL IMPLEMENTATION

Crucial milestones have been achieved on different experimental platforms that pave the way to the implementation of the findings discussed in this work.

Quantum dots (QDs) offer a scalable, highly-tunable solid state platform, in which the control and manipulation of long arrays has already been reached [33–35], including the simulation of fundamental models in condensed matter physics [36]. QDs in c-QED architectures have received a lot of attention in the last years, both theoretically [21, 52–58] and experimentally. The condition $g > \{\kappa, \gamma\}$, usually referred to as strong-coupling regime, has been reached with double QDs [26–28, 59–66], and more recently, in triple QDs as well [24, 67]. The ongoing improvement of the experimental techniques and properties of the QDs has allowed for an optimization of the coupling strength versus the

decoherence rates, and specially charge noise, which has been reduced to only a few MHz [68, 69], while the cavity linewidth normally falls within a range of $\kappa/2\pi \sim 1 - 10$ MHz. On the other hand, the coupling strength can be enhanced by designing microwave cavities with a large characteristic impedance Z_c , since $g \propto \sqrt{Z_c}$ [25]. In hybrid systems including QDs, with energies of the order of GHz, cavities are often realized as coplanar waveguide resonators [70], which give $g/2\pi \sim 20 - 50$ MHz, with exceptions reaching $g/2\pi \sim 200$ MHz [64] owing to the reduced dimensions of the sample. Another option is the employment of arrays of superconducting quantum interference devices (SQUIDs) as cavities, which can have impedances 10^3 times larger than those of coplanar waveguide resonators, as seen in [68] and [25]. In the latter work, the strong coupling regime is reached with $g/2\pi \sim 120$ MHz despite having large decoherence rates around $\kappa/2\pi \sim 12$ MHz and $\gamma/2\pi \sim 40$ MHz. Due to the large dimensions of a QD array, one would expect that the electric field amplitude differs from site to site if it is placed along the axis of the center conductor in the cavity. Then, a spatial modulation of the electric field would be introduced, as modelled by the coupling fermionic operator Z in this work.

Another suitable option for implementation could be cold atoms, where the simulation of complex Hamiltonians with non-trivial topological properties has already been studied [44] and implemented [45]. When placed inside high-finesse cavities [46], they offer great versatility and control: atoms can be loaded deterministically, occupying well-defined positions with respect to each other and to the cavity field, which allows to tailor the atom-field coupling on demand [48, 51], as well as long coherence times [50, 51]. The strong-coupling regime has been achieved [37–43, 49–51], with decoherence rates of few MHz for both the cavity and the atom, and coupling rates of 15–32 MHz. Regarding the model Hamiltonian, it is only required to notice that the hopping term can be written as $\sum_{i,j} t_{i,j} \sigma_i^+ \sigma_j^-$ and the fermionic part of the interaction can be mapped to a Zeeman term that changes linearly with the position $\sum_i B_i^z \sigma_i^z$. This can also be extrapolated to trapped ions [47].

With the previous figures of merit in mind, the current state-of-the-art techniques would allow to implement the topological detection method discussed for the small- g regime, in which the transmission can be used as a topological marker if the edge state is occupied (see Fig. 3). Going beyond this regime would imply larger coupling values, which can be envisioned in future hybrid devices involving the solid-state platforms mentioned above.

Lastly, note that the numerical simulations for reasons of clarity used in this work consider $\Omega = 10$ versus a bandwidth of $\Delta = 4$ for the fermionic system in the off-resonant case. However, a similar behaviour as the one obtained in Fig. 4 is expected for a smaller

Ω , provided that it is off-resonant (given that Δ is fixed).

VI. CONCLUSIONS AND OUTLOOK

In this work, we investigate the use of the cavity transmission t_c as a topological marker for different coupling regimes in an hybrid system, composed of a quantum cavity coupled to a fermionic lattice with distinct topological phases. Both the amplitude $|t_c|$ and phase φ can be experimentally measured, carrying information about the fermionic system interacting with the cavity. For this purpose, we have developed a framework combining two perspectives: first, we have employed the retarded photonic Green function to obtain an exact result for t_c for arbitrary coupling strengths; second, we have combined input-output formalism with a MF plus fluctuations analysis to derive an analytical expression whose validity can be extended beyond the small- g regime. Exploring how the interaction affects the topological properties of the fermionic system is also the aim of this work.

To illustrate our results we have considered a topological SSH chain interacting via the dipolar coupling with the cavity. We reproduce the expected results for small g , where it is well-known that the transmission allows for dispersive readout of the properties of the fermionic system. Detecting differences between its phases with distinct topology is possible if the system is initialized in its edge state, due to their transparency to the bulk states: while the cavity can mediate many transitions between the bulk states, the edge states remain isolated from them. One disadvantage of this regime of operation is that the measurement needs to be carried out before thermalization happens, but this could be avoided by filling the fermionic system to half-filling (however, in this case many systems require to account for particle interactions as well).

Beyond the small- g regime, differences between topological phases are enhanced, and importantly, they can be detected for the ground state, indicating that the measurement can be performed when the system has thermalized. This means that the presence of the edge states still has an impact on the cavity transmission, despite the chiral symmetry breaking induced by the coupling. To study this regime in more depth, we have derived an effective Hamiltonian encoding the role of fluctuations to first order. We find a stabilization of the topological phase for larger coupling strengths, in contrast with the fragility to DC electric fields predicted by perturbative approaches for small g .

Finally, we have also studied the entanglement entropy between different partitions of the total system (Fig. 6), and how this quantity connects with the previous results. First, we verify the entanglement between photons and fermions increases as the coupling strength gets larger, which is crucial for many applications of c-QED architectures [71, 72], up to a critical value at which it suddenly drops to zero. We also explored the entanglement between two asymmetric partitions of the SSH chain, once the photonic degrees of freedom have been traced out. This sheds light on how the interaction affects the eigenstates of the chain, and that the entanglement created by the edge states is maintained for large values of the coupling, even after they have penetrated into the bulk bands.

As an outlook, we believe our work provides a solid basis to study topological systems coupled to quantum cavities, while opening the way to complementary research. For example, including the role of electron interactions using a Hubbard term, or developing an effective Hamiltonian to study the resonant case in more depth. Besides, other interaction models for the cavity and fermionic system could be addressed in order to connect with experiments performed on different set-ups, such as having only one of the sites of the fermionic chain connected to the cavity. This would be the case of the already experimental implementation of QD chains coupled to cavities mentioned in the former section. Lastly, the employment of the entanglement entropy to study the effect of the interaction upon the fermionic system sets a precedent in the field, since it is usually used to characterize topology in non-interacting systems.

Acknowledgements

We thank M. Benito and S. Kohler for fruitful discussions.

This work was supported by: Ministerio de Economía y Competitividad, through Grant MAT2017- 86717-P (CSIC Research Platform PTI-001), Ministerio de Educación y Formación Profesional, under the program FPU, with reference FPU17/05297 (B. P.-G.), the Spanish project PGC2018-094792-B-100 (MCIU/AEI/FEDER, EU) (A. G.-L.). B.P.G. did the analytical and numerical analysis under the supervision of A.G.L. and G.P. All authors discussed and analyzed the results and all authors wrote the paper.

The authors declare that they do not have any competing interests.

[1] H. Walther, B. T. H. Varcoe, B. G. Englert, T. Becker, Cavity quantum electrodynamics, *Rep. Prog. Phys.* **69**,

1325-1382 (2006)

[2] A. Cottet, M. C. Dartiailh, M. M. Desjardins, T.

- Cubaynes, L. C. Contamin, M. Delbecq, J. J. Viennot, L. E. Bruhat, B. Douçot, T. Kontos, Cavity QED with hybrid nanocircuits: from atomic-like physics to condensed matter phenomena, *J. Phys.: Condens. Matter* **29**, 3002-3034 (2017)
- [3] R. H. Dicke, Coherence in spontaneous radiation processes, *Phys. Rev.* **93**, 99-110 (1954)
- [4] J. Li, M. Eckstein, Manipulating Intertwined Orders in Solids with Quantum Light, *Phys. Rev. Lett.* **125**, 217402 (2020)
- [5] A. Blais, R. Huang, A. Wallraff, S. M. Girvin, R. J. Schoelkopf, Cavity quantum electrodynamics for superconducting electrical circuits: an architecture for quantum computation, *Phys. Rev. A* **69**, 062320 (2004)
- [6] T. Pellizzari, S. A. Gardiner, J. I. Cirac, P. Zoller, Decoherence, Continuous Observation, and Quantum Computing: A Cavity QED Model, *Phys. Rev. Lett.* **75**, 3788-3791 (1995)
- [7] A. Blais, J. Gambetta, A. Wallraff, D. I. Schuster, S. M. Girvin, M. H. Devoret, R. J. Schoelkopf, Quantum-information processing with circuit quantum electrodynamics, *Phys. Rev. A* **75**, 032329 (2007)
- [8] D. N. Marsukevich, A. Kuzmich, Quantum state transfer between matter and light, *Science* **306**, 663-666 (2004)
- [9] J. I. Cirac, P. Zoller, H. J. Kimble, H. Mabuchi, Quantum State Transfer and Entanglement Distribution among Distant Nodes in a Quantum Network, *Phys. Rev. Lett.* **78**, 3221-3224 (1997)
- [10] C. A. Downing, T. J. Sturges, G. Weick, M. Stobińska, L. Martín-Moreno, Topological Phases of Polaritons in a Cavity Waveguide, *Phys. Rev. Lett.* **123**, 217401 (2019)
- [11] W. Nie, Y. Liu, Bandgap-assisted quantum control of topological edge states in a cavity, *Phys. Rev. Research* **2**, 012076 (2020)
- [12] M. C. Dartiailh, T. Kontos, B. Douçot, Benoit, A. Cottet, Direct Cavity Detection of Majorana Pairs, *Phys. Rev. Lett.* **118**, 126803 (2017)
- [13] O. Dmytruk, M. Trif, P. Simon, Cavity quantum electrodynamics with mesoscopic topological superconductors, *Phys. Rev. B* **92**, 245432 (2015)
- [14] M. J. Collett, C. W. Gardiner, Squeezing of intracavity and traveling-wave light fields produced in parametric amplification, *Phys. Rev. A* **30**, 1386-1391 (1984)
- [15] C. Gardiner, P. Zoller, *Quantum Noise*, (Springer-Verlag, Berlin, ed. 2, 2000).
- [16] B. Pérez-González, M. Bello, A. Gómez-León, G. Platero, Interplay between long-range hopping and disorder in topological systems, *Phys. Rev. B* **99**, 035146 (2019)
- [17] B. Pérez-González, M. Bello, G. Platero, A. Gómez-León, Simulation of 1D Topological Phases in Driven Quantum Dot Arrays, *Phys. Rev. Lett.* **123**, 126401 (2019)
- [18] M. Bello, C. Creffield, G. Platero, Long-range doublon transfer in a dimer chain induced by topology and ac fields, *Sci. Rep.* **6**, 22562 (2016)
- [19] J. Zhang, Y. Liu, R. Wu, K. Jacobs, F. Nori, *Phys. Rev. A* **87**, 032117 (2013)
- [20] C. Ciuti, I. Carusotto, Input-output theory of cavities in the ultrastrong coupling regime: The case of time-independent cavity parameters, *Phys. Rev. A* **74**, 033811 (2006)
- [21] S. Kohler, Dispersive readout: Universal theory beyond the rotating-wave approximation, *Phys. Rev. A* **98**, 023849 (2018)
- [22] A. Cottet, T. Kontos, B. Douçot, Electron-photon coupling in mesoscopic quantum electrodynamics, *Phys. Rev. B* **91**, 205417 (2015)
- [23] D. F. Walls, G. J. Milburn, *Quantum Optics*, (Springer-Verlag, Berlin, ed. 2, 2008).
- [24] A. J. Landig, J. V. Koski, P. Scalino, U. C. Mendes, A. Blais, C. Reichl, W. Wegscheider, A. Wallraff, K. Ensslin, T. Ihn, Coherent spin-photon coupling using a resonant exchange qubit, *Nature* **560**, 179-184 (2018)
- [25] A. Stockklauser, P. Scarlino, J. V. Koski, S. Gasparinetti, C. K. Andersen, C. Reichl, W. Wegscheider, T. Ihn, K. Ensslin, A. Wallraff, Strong Coupling Cavity QED with Gate-Defined Double Quantum Dots Enabled by a High Impedance Resonator, *Phys. Rev. X* **7**, 011030 (2017)
- [26] X. Mi, M. Benito, S. Putz, S. D. M. Zajac, J. M. Taylor, G. Burkard, J. R. Petta, A coherent spin-photon interface in silicon, *Nature* **555**, 590-603 (2018)
- [27] N. Samkharadze, G. Zheng, N. Kalhor, D. Brousse, A. Sammak, U. C. Mendes, A. Blais, G. Scappucci, L. M. K. Vandersypen, Strong spin-photon coupling in silicon, *Science* **359**, 1123-1127 (2018)
- [28] X. Mi, J. M. Cady, D. M. Zajac, P. W. Deelman, J. R. Petta, Strong coupling of a single electron in silicon to a microwave photon, *Science* **355**, 156-158 (2017)
- [29] S. Ryu, Y. Hatsugai, Entanglement entropy and the Berry phase in the solid state, *Phys. Rev. B* **73**, 245115 (2006)
- [30] V. Gurarie, Single-particle Green's functions and interacting topological insulators, *Phys. Rev. B* **83**, 085426 (2011)
- [31] S. R. Manmana, A. M. Essin, R. M. Noack, V. Gurarie, Topological invariants and interacting one-dimensional fermionic systems, *Phys. Rev. B* **86**, 205119 (2012)
- [32] A. Gómez-León, Hierarchy of correlations: Application to Green's functions and interacting topological phases, *Phys. Rev. B* **94**, 035144 (2016)
- [33] D. M. Zajac, T. M. Hazard, X. Mi, E. Nielsen, J. R. Petta, *Phys. Rev. Applied* **6**, 054013 (2016)
- [34] C. Volk, A. M. J. Zwerver, U. Mukhopadhyay, P. T. Eendebak, C. J. van Diepen, J. P. Dehollain, T. Hensgens, T. Fujita, C. Reichl, W. Wegscheider, L. M. K. Vandersypen, Loading a quantum-dot based "Qubyte" register, *npj Quantum Information* **5**, 29 (2019)
- [35] W. I. L. Lawrie, H. G. J. Eenink, N. W. Hendrickx, J. M. Boter, L. Petit, S. V. Amitonov, M. Lodari, B. Paquette, C. Volk, S. G. J. Philips, G. Droulers, N. Kalhor, F. van Riggelen, D. Brousse, A. Sammak, L. M. K. Vandersypen, G. Scappucci, M. Veldhorst, Quantum dot arrays in silicon and germanium, *Appl. Phys. Lett.* **116**, 080501 (2020)
- [36] T. Hensgens, T. Fujita, L. Janssen, X. Li, C. J. Van Diepen, C. Reichl, W. Wegscheider, S. Das Sarma, L. M. K. Vandersypen, Quantum simulation of a Fermi-Hubbard model using a semiconductor quantum dot array, *Nature* **548**, 70-73 (2017)
- [37] A. Boca, R. Miller, K. M. Birnbaum, A. D. Boozer, J. McKeever, H. J. Kimble, Observation of the Vacuum Rabi Spectrum for One Trapped Atom, *Phys. Rev. Lett.* **93**, 233603 (2004)
- [38] P. Maunz, T. Puppe, I. Schuster, N. Syassen, P. W. H. Pinkse, G. Rempe, Cavity cooling of a single atom, *Nature* **428**, 50-52 (2004)
- [39] J. McKeever, J. R. Buck, A. D. Boozer, H. J. Kimble, Determination of the Number of Atoms Trapped in an Optical Cavity, *Phys. Rev. Lett.* **93**, 143601 (2004)

- [40] J. McKeever, A. Boca, A. D. Boozer, R. Miller, J. R. Buck, A. Kuzmich, H. J. Kimble, Deterministic Generation of Single Photons from One Atom Trapped in a Cavity, *Science* **303**, 1992-1994 (2004)
- [41] J. A. Sauer, K. M. Fortier, M. S. Chang, C. D. Hamley, M. S. Chapman, Cavity QED with optically transported atoms, *Phys. Rev. A* **69**, 051804 (2004)
- [42] J. McKeever, J. R. Buck, A. D. Boozer, A. Kuzmich, H.-C. Nägerl, D. M. Stamper-Kurn, H. J. Kimble, State-Insensitive Cooling and Trapping of Single Atoms in an Optical Cavity, *Phys. Rev. Lett.* **90**, 133602 (2003)
- [43] J. Ye, D. W. Vernoooy, H. J. Kimble, Trapping of Single Atoms in Cavity QED, *Phys. Rev. Lett.* **83**, 4987-4990 (1999)
- [44] D. Zhang, Y. Zhu, Y. X. Zhao, H. Y. Zhu, S. Zhu, Topological quantum matter with cold atoms, *Advances in Physics* **67**, 253-402 (2018)
- [45] M. Atala, M. Aidelsburger, J. T. Barreiro, D. Abanin, T. Kitagawa, E. Demler, I. Bloch, Direct measurement of the Zak phase in topological Bloch bands, *Nature Physics* **9**, 795-800 (2013)
- [46] H. Ritsch, P. Domokos, F. Brennecke, T. Esslinger, Cold atoms in cavity-generated dynamical optical potentials, *Rev. Mod. Phys.* **85**, 553-601 (2013)
- [47] V. Bužek, G. Drobný, M. S. Kim, G. Adam, P. L. Knight, Cavity QED with cold trapped ions, *Phys. Rev. A* **56**, 2352-2360 (1997)
- [48] S. Nußmann, M. Hijkema, B. Weber, F. Rohde, G. Rempe, A. Kuhn, Submicron Positioning of Single Atoms in a Microcavity, *Phys. Rev. Lett.* **95**, 173602 (2005)
- [49] A. D. Boozer, A. Boca, R. Miller, T. E. Northup, H. J. Kimble, Cooling to the Ground State of Axial Motion for One Atom Strongly Coupled to an Optical Cavity, *Phys. Rev. Lett.* **97**, 083602 (2006)
- [50] S. Nußmann, K. Murr, M. Hijkema, B. Weber, A. Kuhn, G. Rempe, Vacuum-stimulated cooling of single atoms in three dimensions, *Nature Physics* **1**, 122-125 (2005)
- [51] K. M. Fortier, S. Y. Kim, M. J. Gibbons, P. Ahmadi, M. S. Chapman, Deterministic Loading of Individual Atoms to a High-Finesse Optical Cavity, *Phys. Rev. Lett.* **98**, 233601 (2007)
- [52] F. P. Laussy, E. del Valle, C. Tejedor, Strong Coupling of Quantum Dots in Microcavities, *Phys. Rev. Lett.* **101**, 083601 (2008)
- [53] M. Benito, X. Mi, J. M. Taylor, J. R. Petta, G. Burkard, *Phys. Rev. B* **96**, 235434 (2017)
- [54] S. Kohler, Dispersive Readout of Adiabatic Phases, *Phys. Rev. Lett.* **119**, 196802 (2017)
- [55] G. Burkard, J. R. Petta, Dispersive readout of valley splittings in cavity-coupled silicon quantum dots, *Phys. Rev. B* **94**, 195305 (2016)
- [56] A. Cottet, C. Mora, T. Kontos, Mesoscopic admittance of a double quantum dot, *Phys. Rev. B* **83**, 121311 (2011)
- [57] M. Schiró, K. Le Hur, Tunable hybrid quantum electrodynamics from nonlinear electron transport, *Phys. Rev. B* **89**, 195127 (2014)
- [58] M. Trif, V. Golovach, D. Loss, Spin dynamics in InAs nanowire quantum dots coupled to a transmission line, *Phys. Rev. B* **77**, 045434 (2008)
- [59] A. Stockklauser, P. Scarlino, J. V. Koski, S. Gasparinetti, C. K. Andersen, C. Reichl, W. Wegscheider, T. Ihn, K. Ensslin, A. Wallraff, Strong Coupling Cavity QED with Gate-Defined Double Quantum Dots Enabled by a High Impedance Resonator, *Phys. Rev. X* **7**, 011030 (2017)
- [60] L. E. Bruhat, T. Cubaynes, J. J. Viennot, M. C. Dartiailh, M. M. Desjardins, A. Cottet, T. Kontos, *Phys. Rev. B* **98**, 155313 (2018)
- [61] D. J. van Woerkom, P. Scarlino, J. H. Ungerer, C. Müller, J. V. Koski, A. J. Landig, C. Reichl, W. Wegscheider, T. Ihn, K. Ensslin, A. Wallraff, Microwave Photon-Mediated Interactions between Semiconductor Qubits, *Phys. Rev. X* **8**, 041018 (2018)
- [62] B. Wang, T. Lin, H. Li, S. Gu, M. Chen, G. Guo, H. Jiang, X. Hu, G. Cao, G. Guo, Correlated spectrum of distant semiconductor qubits coupled by microwave photons, *Science Bulletin* **66**, 332-338 (2021)
- [63] D. Najer, I. Söller, P. Sekatski, V. Dolique, M. C. Löbl, D. Riedel, R. Schott, S. Starsielec, S. R. Valentin, A. Wieck, N. Sangouard, A. Ludwig, R. J. Warbutton, *Nature* **5**, 622-627 (2019)
- [64] N. Samkharadze, G. Zheng, N. Kalhor, D. Brousse, A. Sammak, U. C. Mendes, A. Blais, G. Scappucci, L. M. K. Vandersypen, Strong spin-photon coupling in silicon, *Science* **359**, 1123-1127 (2018)
- [65] T. Cubaynes, M. R. Delbecq, M. C. Dartiailh, R. Assouly, M. M. Desjardins, L. C. Contamin, L. E. Bruhat, Z. Leghtas, F. Mallet, A. Cottet, T. Kontos, Highly coherent spin states in carbon nanotubes coupled to cavity photons, *npj Quantum Information* **5**, 47 (2019)
- [66] F. Borjans, X. G. Croot, X. Mi, M. J. Gullans, J. R. Petta, Resonant microwave-mediated interactions between distant electron spins, *Nature* **577**, 195-198 (2020)
- [67] A. J. Landig, J. V. Koski, P. Scarlino, C. Müller, J. C. Abadillo-Uriel, B. Kratochwil, C. Reichl, W. Wegscheider, S. N. Coppersmith, M. Friesen, A. Wallraff, T. Ihn, K. Ensslin, Virtual-photon-mediated spin-qubit-transmon coupling, *Nature Communications* **10**, 5037 (2019)
- [68] D. J. van Woerkom, P. Scarlino, J. H. Ungerer, C. Müller, J. V. Koski, A. J. Landig, C. Reichl, W. Wegscheider, T. Ihn, K. Ensslin, A. Wallraff, Microwave Photon-Mediated Interactions between Semiconductor Qubits, *Phys. Rev. X* **8**, 041018 (2018)
- [69] X. Mi, J. V. Cady, D. M. Zajac, P. W. Deelman, J. R. Petta, Strong coupling of a single electron in silicon to a microwave photon, *Science* **355**, 156-158 (2017)
- [70] M. Göppl, A. Fragner, M. Baur, R. Bianchetti, S. Filipp, J. M. Fink, P. J. Leek, G. Puebla, L. Steffen, A. Wallraff, Coplanar waveguide resonators for circuit quantum electrodynamics, *Journal of Applied Physics* **104**, 113904 (2008)
- [71] H. J. Kimble, The Quantum Internet, *Nature* **453**, 1023-1030 (2008)
- [72] J. M. Raimond, M. Brune, S. Haroche, Manipulating quantum entanglement with atoms and photons in a cavity, *Rev. Mod. Phys.* **73**, 565-582 (2001)
- [73] See Supplemental Material at [URL] for further details of the calculations and additional numerical results.

SUPPLEMENTAL MATERIALS

Appendix A: Input-output formalism

Using the initial Hamiltonian

Consider the initial Hamiltonian describing a transmission line with two ports, coupled to the topological system via the cavity photons. The total Hamiltonian is:

$$H = \Omega d^\dagger d + H_S + g(d^\dagger + d)Z + H_B, \quad (\text{A1})$$

with H_B being the Hamiltonian for the electromagnetic field in the transmission line and its coupling to the cavity, as described in the main text. The first step is to derive the equation of motion (EoM) for the transmission line photons:

$$\frac{d}{dt}b_l(\nu, t) = -i\nu b_l(\nu, t) + \sqrt{\frac{\kappa_l}{2\pi}}d(t) \quad (\text{A2})$$

which can be formally integrated to yield

$$b_l(\nu, t) = b_l(\nu, t_0)e^{-i\nu(t-t_0)} + \sqrt{\frac{\kappa_l}{2\pi}} \int_{t_0}^t dt' e^{-i\nu(t-t')} d(t') \quad (\text{A3})$$

where $t_0 < t$ represents the initial condition. Inserting the previous expression into the EoM for the cavity photons, we get

$$\begin{aligned} \frac{d}{dt}d(t) &= -i\Omega d(t) - igZ(t) - \sum_{l=1,2} \sqrt{\frac{\kappa_l}{2\pi}} \int_{-\infty}^{\infty} d\nu b_l(\nu, t) \\ &= -i\left(\Omega - i\frac{\kappa}{2}\right)d(t) - igZ(t) \\ &\quad - \sum_{l=1,2} \sqrt{\kappa_l} b_{in,l}(t) \end{aligned} \quad (\text{A4})$$

where $\kappa = \kappa_1 + \kappa_2$ and we have defined an input field,

$$b_{in,l}(t) = \frac{1}{\sqrt{2\pi}} \int_{-\infty}^{\infty} b_l(\nu, t_0) e^{-i\nu(t-t_0)} d\nu. \quad (\text{A5})$$

Similarly, the solution for $b_l(\nu, t)$ in (A3) can also be obtained in terms of a final condition $t_1 > t$, which let us define an output field $b_{out,l}(t)$, fulfilling

$$b_{out,l}(t) = b_{in,l}(t) + \sqrt{\kappa_l}d(t) \quad (\text{A6})$$

One has to solve the EoM for $Z(t)$ as well. We consider the basis of eigenstates of the fermionic Hamiltonian

$$H_S = \sum_{\alpha=1}^N E_\alpha X^{\alpha,\alpha}, \quad Z = \sum_{\bar{\alpha}} Z_{\bar{\alpha}} X^{\bar{\alpha}} \quad (\text{A7})$$

with $X^{\bar{\alpha}} = X^{\alpha_1, \alpha_2} = |\alpha_1\rangle\langle\alpha_2|$, and calculate the equation of motion for an arbitrary Hubbard operator $X^{\bar{\alpha}}$

$$\begin{aligned} \partial_t \tilde{X}^{\bar{\alpha}}(t) &= i\left(\tilde{E}_{\bar{\alpha}} - i\frac{\gamma}{2}\right) \tilde{X}^{\bar{\alpha}}(t) \\ &\quad + ig(d^\dagger(t) + d(t)) \sum_{\beta} \left(\tilde{Z}_{\beta, \alpha_1} \tilde{X}^{\beta, \alpha_2}(t) \right. \\ &\quad \left. - \tilde{Z}_{\alpha_2, \beta} \tilde{X}^{\alpha_1, \beta}(t) \right), \end{aligned} \quad (\text{A8})$$

where $E_{\bar{\alpha}} = E_{\alpha_1} - E_{\alpha_2}$ and we have also included the phenomenological spectral broadening factor $\gamma/2$. The product $d^{(\dagger)}(t)X(t)$ can be decomposed as

$$d^{(\dagger)}(t)X(t) \approx \langle X \rangle d^{(\dagger)}(t) + \langle d^{(\dagger)} \rangle X(t), \quad (\text{A9})$$

where we are neglecting any terms accounting for correlation between operators, which is true in the small- g regime. Under this condition, one can safely calculate $\langle X \rangle$ and $\langle d^{(\dagger)} \rangle$ using the corresponding unperturbed Hamiltonians, H_S and $\Omega d^\dagger d$, respectively. Then, one can easily see that $\langle d^{(\dagger)} \rangle = 0$, and hence the solution for the EoM in (A8) in frequency space reads

$$X^{\bar{\alpha}}(\omega) \simeq gd(\omega) \frac{\sum_{\beta} (Z_{\alpha_2, \beta} \langle X^{\alpha_1, \beta} \rangle - Z_{\beta, \alpha_1} \langle X^{\beta, \alpha_2} \rangle)}{\omega + E_{\bar{\alpha}} - i\frac{\gamma}{2}}. \quad (\text{A10})$$

We have also neglected the contribution of $\langle X \rangle d^\dagger(\omega)$, as typically done in the literature [21]. Substituting this result in (A4), we find

$$d(\omega) = \frac{i \sum_{l=1,2} \sqrt{\kappa_l} b_{in,l}(\omega)}{\Omega - \omega - i\frac{\kappa}{2} + g^2 \chi(\omega)} \quad (\text{A11})$$

where

$$\chi(\omega) = \sum_{\bar{\alpha}, \beta} \frac{Z_{\bar{\alpha}} (Z_{\alpha_2, \beta} \langle X^{\alpha_1, \beta} \rangle - Z_{\beta, \alpha_1} \langle X^{\beta, \alpha_2} \rangle)}{\omega + E_{\bar{\alpha}} - i\frac{\gamma}{2}}. \quad (\text{A12})$$

Using (A6), and taking into account that the input is inserted through the left port ($l = 1$) into the cavity, and

the output is collected through the right one ($l = 2$), we can write the transmission as

$$t_c(\omega) = \frac{\langle b_{\text{out},2} \rangle}{\langle b_{\text{in},1} \rangle} = \frac{i\sqrt{\kappa_1\kappa_2}}{\Omega - \omega - i\frac{\kappa}{2} + g^2\chi(\omega)} \quad (\text{A13})$$

which is the usual result for the cavity transmission, with $\chi(\omega)$ being the electronic susceptibility.

Using the mean-field Hamiltonian

If we instead consider the MF Hamiltonian for the cavity, topological system and their interaction, we start from the following expression

$$\begin{aligned} H = & \Omega d^\dagger d - \frac{g^2\langle Z \rangle^2}{\Omega} + \tilde{H}_S + g(d^\dagger + d)\tilde{Z} \\ & + \sum_{l=1,2} \int_{-\infty}^{\infty} \omega b_l^\dagger(\omega) b_l(\omega) d\omega \\ & + i \sum_{l=1,2} \sqrt{\frac{\gamma_l}{2\pi}} \int_{-\infty}^{\infty} d\omega \left[b_l^\dagger(\omega) \left(d - \frac{g\langle Z \rangle}{\Omega} \right) \right. \\ & \quad \left. - \left(d^\dagger - \frac{g\langle Z \rangle}{\Omega} \right) b_l(\omega) \right] \quad (\text{A14}) \end{aligned}$$

where $\tilde{Z} = Z - \langle Z \rangle$ and $\tilde{H}_S = H_S - \frac{2g^2\langle Z \rangle}{\Omega} Z$. Note that the cavity operators have been rotated to $\tilde{d}^{(\dagger)} = d^{(\dagger)} - \frac{g\langle Z \rangle}{\Omega}$ in order to diagonalize their MF Hamiltonian. The self-consistent values of $\langle Z \rangle$ and $\langle d^{(\dagger)} \rangle$ have been determined ignoring the coupling to the transmission line, as explained in the main text. Importantly, the cavity operators in H_B have also been rotated accordingly. This time, the EoM for $b_l(\nu, t)$ yields the following solution

$$\tilde{b}_l(\nu, t) = b_l(\nu, t) - \frac{g\langle Z \rangle}{\Omega} \sqrt{\frac{\kappa_l}{2\pi}} \frac{1 - e^{-i\nu(t-t_0)}}{i\nu} \quad (\text{A15})$$

Compared to (A3), we have an extra term due to the rotation of the bosonic operators, that depends on the state of the fermionic system through $\langle Z \rangle$. The EoM for $a(t)$ has the same form, with redefined input and output fields

$$\tilde{b}_{\text{in},l}(t) = b_{\text{in},l}(t) - \frac{g\sqrt{\kappa_l}\langle Z \rangle}{2\pi\Omega} \int_{-\infty}^{\infty} \frac{1 - e^{-i\nu(t-t_0)}}{i\nu} d\nu, \quad (\text{A16})$$

$$\tilde{b}_{\text{out},l}(t) = b_{\text{out},l}(t) + \frac{g\sqrt{\kappa_l}\langle Z \rangle}{2\pi\Omega} \int_{-\infty}^{\infty} \frac{1 - e^{i\nu(t_1-t)}}{i\nu} d\nu, \quad (\text{A17})$$

also fulfilling that $\tilde{b}_{\text{out},l}(t) = \tilde{b}_{\text{in},l}(t) + \sqrt{\kappa_l}d(t)$. On the other hand, the Hubbard operators change as well due to the presence of the extra MF contribution in the fermionic Hamiltonian

$$\tilde{H}_S = H_S - \frac{2g^2\langle Z \rangle}{\Omega} Z = \sum_{\alpha=1}^N \tilde{E}_\alpha \tilde{X}^{\alpha,\alpha}, \quad (\text{A18})$$

$$\tilde{Z} = \sum_{\tilde{\alpha}} \tilde{Z}_{\tilde{\alpha}} \tilde{X}^{\tilde{\alpha}}. \quad (\text{A19})$$

The EoM for \tilde{X} has the same form of (A8), but substituting the eigenvalues and eigenvectors of the unperturbed fermionic Hamiltonian H_S by the ones of MF Hamiltonian \tilde{H}_S . To solve the EoM, we take fluctuations to be small, which is a valid assumption when g is both small and very large, i.e., when the MF Hamiltonian $\tilde{H}_S + \tilde{H}_\Omega$ accurately describes the physics of the system, without considering the fluctuations Hamiltonian \tilde{H}_δ . Under this condition, we can write $d^{(\dagger)}(t) \tilde{X}(t) \approx \langle \tilde{X} \rangle d^{(\dagger)}(t) + \langle d^{(\dagger)} \rangle \tilde{X}(t)$. Again, we neglect any correlation created by the fluctuations Hamiltonian, which acts as an effective interaction between the two MF Hamiltonians. Note that $\langle d^{(\dagger)} \rangle = 0$ when evaluated using the MF photonic Hamiltonian in the rotated frame, \tilde{H}_Ω . Formally, the decoupling employed to solve (A19) is the same as the one used in (A8). Then, the solution for \tilde{X} gives

$$\tilde{X}^{\tilde{\alpha}}(\omega) \simeq g d(\omega) \frac{\sum_{\beta} \left(\tilde{Z}_{\alpha_2,\beta} \langle \tilde{X}^{\alpha_1,\beta} \rangle - \tilde{Z}_{\beta,\alpha_1} \langle \tilde{X}^{\beta,\alpha_2} \rangle \right)}{\omega + \tilde{E}_{\tilde{\alpha}} - i\frac{\gamma}{2}}. \quad (\text{A20})$$

Note that (A12) is analogous to (A20), but all parameters have been renormalized due to MF. Finally, the transmission can be written as

$$t_c(\omega) = \frac{i\sqrt{\kappa_1\kappa_2}}{\Omega - \omega - i\frac{\kappa}{2} + g^2\tilde{\chi}(\omega)}. \quad (\text{A21})$$

where now $\tilde{\chi}(\omega)$ is the susceptibility written in terms of the MF Hamiltonian.

Appendix B: Transmission and photonic Green's function

The starting point is the EoM for the photonic operator $d(t)$ (A4) in Fourier space

$$\begin{aligned} i\omega d(\omega) = & -i \left(\Omega - i\frac{\kappa}{2} \right) d(\omega) - ig \sum_{\tilde{\alpha}} Z_{\tilde{\alpha}} \tilde{X}^{\tilde{\alpha}}(\omega) \\ & - \sum_{l=1,2} \sqrt{\kappa_l} \tilde{b}_{\text{in},l}(\omega) \quad (\text{B1}) \end{aligned}$$

The losses of the cavity have been included through the phenomenological factor κ . This equation depends on $\tilde{X}^{\tilde{\alpha}}(\omega)$, which has its own dynamics as well,

$$\begin{aligned} i\omega \tilde{X}^{ij}(\omega) &= -i \left(E_j - E_i + i\frac{\gamma}{2} \right) \tilde{X}^{ij}(\omega) \\ &\quad - ig \left(d^\dagger(\omega) + d(\omega) \right) \sum_m \left(Z_{jm} \tilde{X}^{im}(\omega) \right. \\ &\quad \left. - Z_{mi} \tilde{X}^{mj}(\omega) \right). \end{aligned} \quad (\text{B2})$$

Solving this equation implies writing the EoM for $a^{(\dagger)} X^{ij}$, which at the same time is coupled to higher-order operators. Then, we can write an infinite vector with all the relevant operators involved, $\vec{v} = (d, X^{ij}, \dots)$, and the system of equations turns out to be

$$(\omega - A) \vec{v} = \vec{v}_0 \quad (\text{B3})$$

where A is the coefficients matrix and \vec{v}_0 represents the inhomogeneous term.

Then, on the other hand, we can write the EoM for the retarded photonic Green function, defined as $G(t) = -i\theta(t) \langle [a(t), a^\dagger] \rangle \equiv \langle \langle a(t); a^\dagger \rangle \rangle_t$, yielding

$$i\omega G(\omega) = 1 + \left(\Omega - i\frac{\kappa}{2} \right) \tilde{G}(\omega) + g \sum_{ij} M_{ij}(\omega) \quad (\text{B4})$$

where $\tilde{M}_{ij}(\omega) = \langle \langle X^{ij}; a^\dagger \rangle \rangle_\omega$. Again, this EoM is coupled to higher-order Green functions, resulting in an infinite system of coupled differential equations. In matrix form, we have

$$(\omega - A') \vec{V}(\omega) = \vec{V}_0 \quad (\text{B5})$$

where $\vec{V} = (G, M_{ij}, \dots)$ and \vec{V}_0 is the inhomogeneous term by comparison. One can see that $A = A'$, which indicates that $G(\omega) = -i\theta(t) \langle [a(t), a^\dagger] \rangle$ is the resolvent of (B1).

Finally, we can compare the first component of each system of equations, namely $a(\omega) = -i(\omega - H)^{-1} \sum_{l=1,2} \sqrt{\kappa_l} \tilde{b}_{in,l}(\omega)$ and $G(\omega) = (\omega - H)^{-1}$, and see that

$$a(\omega) = -iG(\omega) \sum_{l=1,2} \sqrt{\kappa_l} \tilde{b}_{in,l}(\omega). \quad (\text{B6})$$

The last step is to write the transmission as a function of $a(\omega)$, knowing that $\tilde{b}_{out,l}(t) = \tilde{b}_{in,l}(\omega) + \sqrt{\kappa_l} a(\omega)$ and that the only input is through port 1

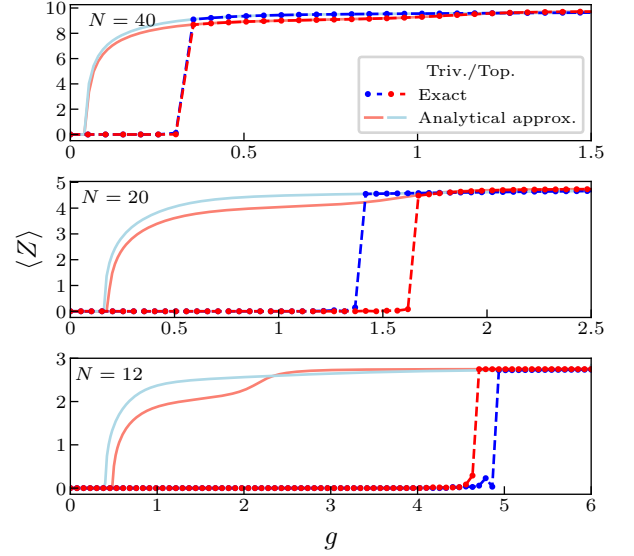


Figure 7: $\langle Z \rangle$ for different N . $\langle Z \rangle$ as a function of the coupling constant g for $\Omega = 10$, $\delta = \pm 0.6$ (trivial/topological phase) and different system sizes: $N = 40$ (top), $N = 20$ (middle), $N = 12$ (bottom). The value of $\langle Z \rangle$ has been calculated self-consistently using mean field (solid) and exact diagonalization (dashes and dots). The chain size modifies the value of the critical point at which the system polarizes, enhancing or reducing the difference between topological phases at the phase transition

$$t_c = \frac{\langle \tilde{b}_{out,2} \rangle}{\langle \tilde{b}_{in,1} \rangle} = \frac{\langle \tilde{b}_{in,2} \rangle + \sqrt{\kappa_2} \langle a \rangle}{\langle \tilde{b}_{in,1} \rangle} = -i\sqrt{\kappa_2} \sqrt{\kappa_1} G(\omega) \quad (\text{B7})$$

Appendix C: $\langle Z \rangle$ as a function of N

The size of the fermionic chain affects the phase diagram for the order parameter $\langle Z \rangle$. As the number of sites N increases, the critical value of the coupling constant at which the phase transition happens is reduced (see Fig. 7). This is expected, since the effective strength of the coupling at each site $g_i = gx_i$ gets larger as more sites are considered.

The system size also shapes the differences between topological phases found immediately after the phase transition, that are captured by the MF calculation, without including fluctuations.

Appendix D: Resonant case for arbitrary coupling

The exact transmission coefficient for the resonant case can be evaluated numerically using the photonic propagator and Eq. 11 from the main text. However, the presence of highly-correlated hybrid states compromises

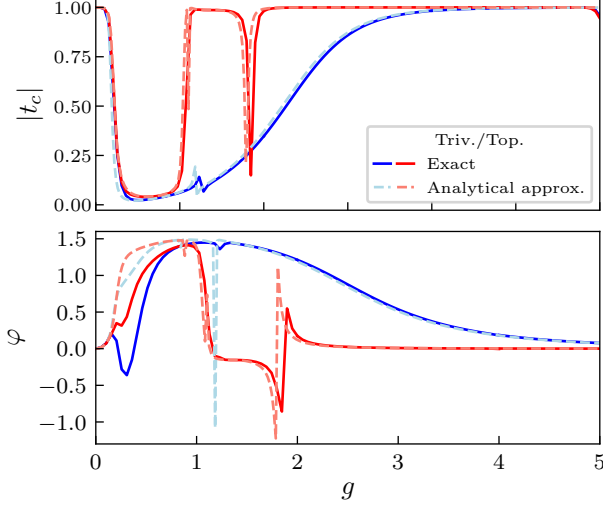


Figure 8: $|t_c(\omega)|$ and φ as a function of g for the resonant case. Dashed lines indicate the solution from the analytical approximation (Eq. 17), while solid lines correspond to the exact solution (Eq. 11). We consider the ground state of the chain ($N = 20$) is occupied. The parameters used are: $\Omega = 3.6$, $|\delta| = 0.8$

the analytical expression in Eq. 17 for larger values of the coupling constant. A preliminary result evaluating Eq. 17 is shown in fig. 8, where we plot the cavity transmission for $\Omega = 3.6$ and $|\delta| = 0.8$, where the cavity frequency corresponds to the energy distance between the ground state and the bottom state in the conduction band. We see then that the behaviour of $|t_c|$ is very well captured even under these circumstances, and the comparison with the results for φ shows that measuring $|t_c|$ is more reliable in this case.

Appendix E: Schrieffer-Wolff transformation

We begin from the Hamiltonian $H = H_0 + V$ in the basis of localized states:

$$H_0 = \sum_{i,j} t_{i,j} \left(B_i^{1,0} A_j^{0,1} + A_i^{1,0} B_j^{0,1} \right) + \Omega d^\dagger d - \frac{2g^2}{\Omega} \langle Z \rangle \sum_i x_i \left(A_i^{1,1} + B_i^{1,1} \right) \quad (\text{E1})$$

$$V = g (d^\dagger + d) \left[\sum_i x_i \left(A_i^{1,1} + B_i^{1,1} \right) - \langle Z \rangle \right] \quad (\text{E2})$$

where $H_0 = \tilde{H}_S + \tilde{H}_\Omega$ corresponds to the MF Hamiltonian in the diagonal basis of photons, $V = \tilde{H}_\delta$ to the fluctuations Hamiltonian, and we have defined the transition operators A_i^μ and B_i^μ acting at sub-lattice site A and B, respectively. The MF part contains the usual SSH Hamiltonian, plus a MF term that effectively breaks chiral symmetry, hence opening a gap in the edge states and

spoiling their localization. Our intention is to find out if quantum fluctuations can stabilize the topological phase. For this, we propose the following ansatz for the S-W transformation:

$$S = \sum_{l,r} \left(\Gamma_{l,r}^+ d^\dagger + \Gamma_{l,r}^- d \right) \left(B_l^{1,0} A_r^{0,1} + A_l^{1,0} B_r^{0,1} \right) + \sum_l \left(\Lambda_l^+ d^\dagger + \Lambda_l^- d \right) \left(A_l^{1,1} + B_l^{1,1} \right) + \alpha_+ d^\dagger + \alpha_- d \quad (\text{E3})$$

where imposing $[H_0, S] = V$, one finds the following equations for the free parameters:

$$\sum_l \left(t_{i,l} \Gamma_{l,j}^+ - t_{l,j} \Gamma_{i,l}^+ \right) = 0 \quad (\text{E4})$$

$$t_{i,j} \left(\Lambda_j^\pm - \Lambda_i^\pm \right) \pm \left(\Omega \mp \frac{2g^2}{\Omega} \langle Z \rangle x_{i,j} \right) \Gamma_{i,j}^\pm = 0 \quad (\text{E5})$$

$$\sum_j \left(t_{i,j} \Gamma_{j,i}^\pm - t_{j,i} \Gamma_{i,j}^\pm \right) \pm \Omega \Lambda_i^\pm = g x_i \quad (\text{E6})$$

$$\pm \Omega \alpha_\pm + g \langle Z \rangle = 0 \quad (\text{E7})$$

This results in the following expressions for the free parameters:

$$\Lambda_i^\pm = \pm \frac{g}{\Omega} x_i \quad (\text{E8})$$

$$\Gamma_{i,j}^\pm = \frac{g t_{i,j} x_{i,j}}{\Omega^2 \mp 2g^2 \langle Z \rangle x_{i,j}} \quad (\text{E9})$$

$$\alpha_\pm = \mp \frac{g}{\Omega} \langle Z \rangle \quad (\text{E10})$$

and the final form of the transformation:

$$S = \sum_{i,j} \left(\frac{g t_{i,j} x_{i,j}}{\Omega^2 - 2g^2 \langle Z \rangle x_{i,j}} d^\dagger + \frac{g t_{i,j} x_{i,j}}{\Omega^2 + 2g^2 \langle Z \rangle x_{i,j}} d \right) \cdot \left(B_i^{1,0} A_j^{0,1} + A_i^{1,0} B_j^{0,1} \right) + \frac{g}{\Omega} (d^\dagger - d) \left[\sum_i x_i \left(A_i^{1,1} + B_i^{1,1} \right) - \langle Z \rangle \right] \quad (\text{E11})$$

The correction to the Hamiltonian is proportional to:

$$\begin{aligned}
[S, V] = & g^2 \sum_{i,j} \frac{t_{ij} x_{ij}^2 (4g^2 \langle Z \rangle^2 - \Omega^2)}{\Omega^4 - 4g^4 \langle Z \rangle^2 x_{ij}^2} \\
& \cdot (B_i^{1,0} A_j^{0,1} + A_i^{1,0} B_j^{0,1}) \\
& + \frac{4g^2 \langle Z \rangle}{\Omega} \sum_i x_i (A_i^{1,1} + B_i^{1,1}) - \frac{2g^2 \langle Z \rangle^2}{\Omega} \\
& - d^\dagger d \sum_{i,j} \frac{2\Omega^2 g^2 t_{ij} x_{ij}^2}{\Omega^4 - 4g^4 \langle Z \rangle^2 x_{ij}^2} (B_i^{1,0} A_j^{0,1} + A_i^{1,0} B_j^{0,1}) \\
& - \sum_{i,j} \left(\frac{g^2 t_{ij} x_{ij}^2 (d^\dagger)^2}{\Omega^2 - 2g^2 \langle Z \rangle x_{ij}} + \frac{g^2 t_{ij} x_{ij}^2 d^2}{\Omega^2 + 2g^2 \langle Z \rangle x_{ij}} \right) \\
& \cdot (B_i^{1,0} A_j^{0,1} + A_i^{1,0} B_j^{0,1}) \\
& - 2g^4 \langle Z \rangle \sum_{i,j} \frac{t_{ij} x_{ij}^2}{\Omega^4 - 4g^4 \langle Z \rangle^2 x_{ij}^2} \\
& \cdot \sum_l x_l \{ B_i^{1,0} A_j^{0,1} + A_i^{1,0} B_j^{0,1}, A_l^{1,1} + B_l^{1,1} \} \\
& - \frac{g^2}{\Omega} \sum_{i,l} x_i x_l \{ A_i^{1,1} + B_i^{1,1}, A_l^{1,1} + B_l^{1,1} \} \quad (\text{E12})
\end{aligned}$$

and the effective Hamiltonian can be approximated by:

$$\begin{aligned}
\tilde{H} = & H_0 + \frac{1}{2} [S, V] \\
\approx & \sum_{i,j} \bar{t}_{ij} (B_i^{1,0} A_j^{0,1} + A_i^{1,0} B_j^{0,1}) \\
& + d^\dagger d \left[\Omega - \sum_{i,j} \bar{\Omega}_{ij} (B_i^{1,0} A_j^{0,1} + A_i^{1,0} B_j^{0,1}) \right] \\
& - \sum_{i,j} \bar{\rho}_{ij} \sum_l x_l \{ B_i^{1,0} A_j^{0,1} + A_i^{1,0} B_j^{0,1}, A_l^{1,1} + B_l^{1,1} \} \\
& - \frac{g^2}{2\Omega} \sum_{i,l} x_i x_l \{ A_i^{1,1} + B_i^{1,1}, A_l^{1,1} + B_l^{1,1} \} \quad (\text{E13})
\end{aligned}$$

with the definitions in Eqs. 22 – 24, in the main text.

Finally, one can rewrite \tilde{H} in terms of the creation and annihilation operators, c_m^\dagger and c_m on each site m of the chain, obtaining

$$\begin{aligned}
\bar{H} \approx & \sum_{m,n} \bar{t}_{m,n} c_m^\dagger c_n + \Omega d^\dagger d \left(1 - \sum_{m,n} \bar{\Omega}_{m,n} c_m^\dagger c_n \right) \\
& - \sum_{m,n} \bar{\rho}_{mn} \{ c_m^\dagger c_n, Z \} - \frac{g^2}{2\Omega} \{ Z, Z \}, \quad (\text{E14})
\end{aligned}$$

Appendix F: Entanglement Entropy and Energy Spectrum

As shown in Fig. 6(c) in the main text, there is a log(2)-plateau in the topological phase for small- g when the $N/2$ -th state is occupied, corresponding to one of the topological edge states. Its drop at $g \sim 0.84$ corresponds with its anti-crossing with a state belonging to the bulk bands and indicates the destruction of maximal entanglement for the $N/2$ -th state.

However, the topological contribution to the entanglement entropy is not lost at this point, but migrates from one state to the other as they further anti-cross in the energy spectrum. Figure 9 shows a zoom of the energy spectrum where the edge states penetrate into the bulk bands, together with the entanglement entropy S_A associated to the occupation of each of them. For small- g , the log(2) plateau corresponds to the $N/2$ -th (red) and $(N/2 + 1)$ -th (yellow) states (edge states), while the rest of them are not maximally entangled (their S_A depends on the partition used). The first anti-crossing encountered in the spectrum (at $g \sim 0.78$) between the yellow and blue (top state in the valence band) states, corresponds to the appearance of a log(2)-plateau for the later, while the entanglement between the ending sites is lost for the edge state.

On the other hand, as g is increased, the $N/2$ -th state anti-crosses with other states as well. Figure 10 shows that each of these anti-crossings correspond to the abrupt changes in S_A obtained for the $N/2$ -th state (Fig. 6C), by zooming into the first four of them.

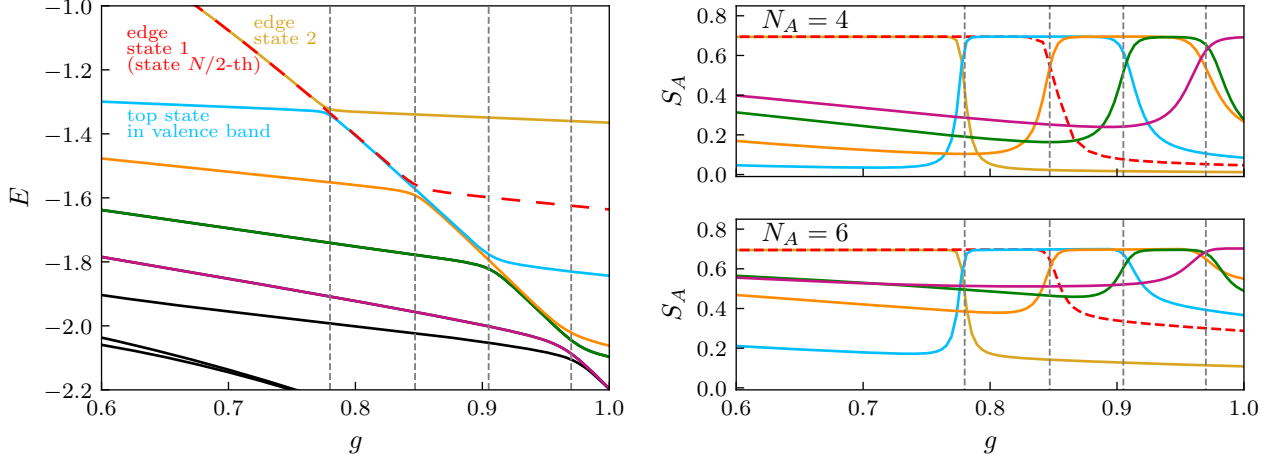


Figure 9: **Entanglement entropy and the energy spectrum.** Left plot: zoom into the energy spectrum, as a function of g , corresponding to the anti-crossing (dashed, grey vertical lines) of energy states triggered by the entrance of the edge states into the bulk band. The parameters chosen are: $\Omega = 10$ $\delta = -0.6$, $N = 20$. Each state is depicted in a different color: yellow for the $(\frac{N}{2} + 1)$ -th state, red for the $N/2$ -th (corresponding to the two edge states), blue for the $(\frac{N}{2} - 1)$ -th (top state in the valence band), orange for the $(\frac{N}{2} - 2)$ -th, green for the $(\frac{N}{2} - 3)$ -th and violet for the $(\frac{N}{2} - 4)$ -th (the following states appear in black). The first anti-crossing at $g \sim 0.78$ happens between the edge state (yellow) and the top state in the valence band (blue). The second anti-crossing at $g \sim 0.9$ happens between the edge state (red) and $(\frac{N}{2} - 2)$ -th state in the bulk band (orange). For higher values of the coupling constant (only shown up to $g = 1$), successive anti-crossings between adjacent states appear. Right plot: entanglement entropy for each state (same color code as in the left plot), for different partitions $N = 4$ (upper plot) and $N = 6$ (lower plot). For small- g , the $\log(2)$ plateau corresponds to the $N/2$ -th state, while the rest of them are not maximally entangled (their S_A depends on the partition used). Each time a state from the bulk band anti-crosses with an edge state, it turns into an edge state itself, so that the $\log(2)$ plateau (originally caused by the non-trivial topology of the fermionic system) migrates from one state to the other.

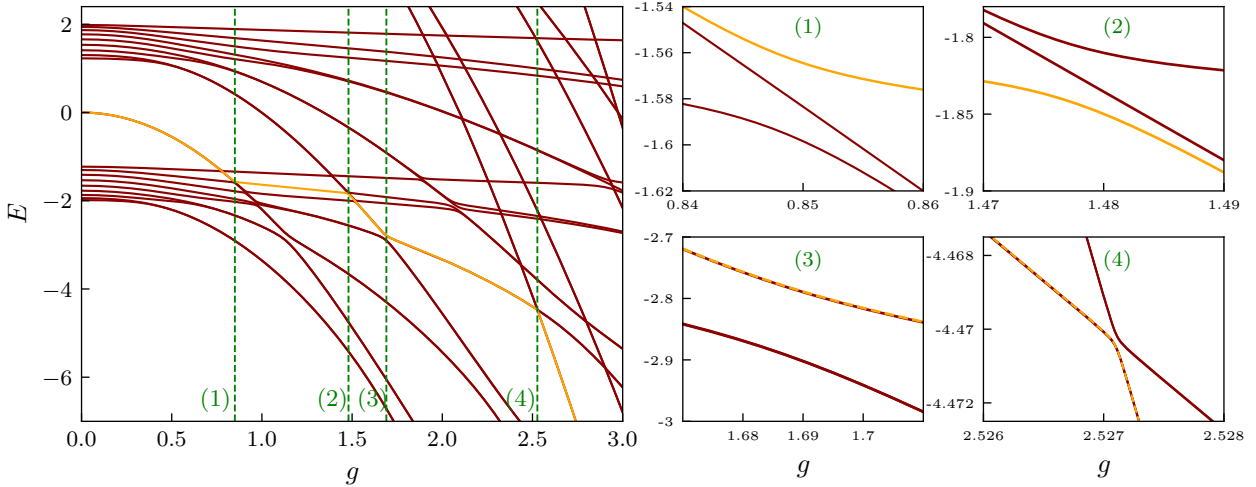


Figure 10: **Anti-crossings for the $N/2^{\text{th}}$ state in the topological phase.** Left plot: energy spectrum for the zero-photon band as a function of g . The $N/2$ -th state (for which the entanglement entropy is calculated in Fig. 6(c)) is represented in orange. The green, dashed lines represent the first four anti-crossings for this state, which correspond to the first four abrupt changes in S_A in Fig. 6(c). Right plots: zoom into the first four anti-crossings of the $N/2$ -th state.